Optimization of graded porous acoustic absorbers based on triply periodic minimal surfaces

Guan, Xueying; Deckers, Elke; Dong, Hao; Hornikx, Maarten; Yang, Jieun

DOI
10.1016/j.matdes.2025.113852

Publication date
2025

Document Version
Final published version

Published in
Materials & Design

Citation (APA)
Guan, X., Deckers, E., Dong, H., Hornikx, M., & Yang, J. (2025). Optimization of graded porous acoustic absorbers based on triply periodic minimal surfaces. *Materials & Design*, *253*, Article 113852. https://doi.org/10.1016/j.matdes.2025.113852

Materials & Design 253 (2025) 113852

Contents lists available at ScienceDirect

Materials & Design

journal homepage: www.elsevier.com/locate/matdes

Optimization of graded porous acoustic absorbers based on triply periodic minimal surfaces

Xueying Guan [a], Elke Deckers [b,c], Hao Dong [d], Maarten Hornikx [e], Jieun Yang [a,*]

[a] Department of Precision and Microsystems Engineering, Faculty of Mechanical Engineering, Delft University of Technology, Mekelweg 2, 2628 CD Delft, The Netherlands

[b] Department of Mechanical Engineering, KU Leuven, Campus Diepenbeek, Wetenschapspark 27, 3590 Diepenbeek, Belgium

[c] Flanders Make@KU Leuven, Belgium

[d] Laboratoire Procédés et Ingénierie en Mécanique et Matériaux (PIMM), Arts et Métiers ParisTech, UMR CNRS 8006, CNAM, HESAM université, 151 Boulevard de l'Hôpital, 75013 Paris, France

[e] Department of the Built Environment, Eindhoven University of Technology, Groene Loper 3, 5612 AE Eindhoven, The Netherlands

ARTICLE INFO

Keywords:
Triply periodic minimal surface
Sound absorption
Porosity grading
Homogenization
Optimization
3D printing

ABSTRACT

The acoustic absorption of a porous structure within a specific frequency range can be tuned by varying its porosity along its thickness. In this work, triply periodic minimal surfaces (TPMS) are employed to generate graded porous structures, where the continuous porosity gradient is controlled by a mathematical function involving geometric parameters. A hybrid homogenization technique, combined with the transfer matrix method (TMM), is used to predict the normal incidence absorption coefficient of the graded TPMS structure. The porosity distribution along the thickness is then optimized using a global search method combined with a local gradient-based solver to maximize acoustic absorption within a target frequency range. The optimization results suggest that a combination of high- and low-porosity layers achieves broadband impedance matching conditions by shifting the so-called quarter-wavelength resonance frequencies. The design of the TPMS absorbers is validated through impedance tube measurements of 3D-printed samples.

1. Introduction

The interaction between the solid and fluid phases in porous materials leads to the dissipation of sound energy through viscous and thermal effects [1]. Hence, the acoustic absorption of a porous material largely depends on its microstructure [2]. Traditional porous foams, with their highly random microstructures, often pose challenges in controlling and predicting their sound absorption performance [3]. Recently, additive manufacturing techniques such as fused deposition modeling (FDM) [4–7], stereolithography (SLA) [8,9], digital light processing (DLP) [10,11] and selective laser melting (SLM) [10,12] have been employed to produce innovative periodic porous materials formed by the repetition of a unit cell. Researchers have proposed and realized sound-absorbing periodic porous materials with different kinds of unit cells, for instance, narrow tubes [13], structures made by the subtraction of spheres from cubic cells [4], orthogonal rods [5–7], plate and truss lattices [14,15], Kelvin cells [10,16], cubic cells with channel-connected spherical pores [8,17], and triply periodic minimal surfaces (TPMS) [9,12]. This enables the customization of the sound absorption spectrum for various applications. A review of these 3D printed sound-absorbing periodic structures can be found in Ref. [18].

The solid phase of a sound-absorbing porous material is often assumed to be rigid, resulting in the material being modeled as an equivalent fluid medium. Consequently, the macroscopic characterization of the acoustic properties of the porous material involves determining an effective density, $\rho_e(\omega)$, which accounts for inertial and viscous dissipation, and an effective bulk modulus, $K_e(\omega)$, which accounts for thermal dissipation [19]. In the case of a periodic porous material, these macroscopic properties can be derived from boundary value problems at the microscale over a representative elementary volume (REV) (in this case the periodic unit cell) with the multiscale homogenization method [20]. A number of recent studies on periodic porous materials [4,6,20] numerically calculate transport parameters from the REV with finite element simulations. These transport parameters are then used as inputs for

* Corresponding author.
E-mail address: jieun.yang@tudelft.nl (J. Yang).

https://doi.org/10.1016/j.matdes.2025.113852
Received 29 January 2025; Received in revised form 12 March 2025; Accepted 17 March 2025

Available online 21 March 2025

semi-phenomenological models such as the Johnson-Champoux-Allard-Lafarge (JCAL) model [21–23] to obtain the effective density $\rho_e(\omega)$ and effective bulk modulus $K_e(\omega)$.

Graded and multilayer structures are common ways to enhance the broadband sound absorption [24,25]. A monotonically increasing airflow resistivity (or decreasing porosity) along the thickness of the porous material is believed to improve the impedance matching of acoustic absorbers with the surrounding medium [26]. A number of recent studies on 3D-printed periodic porous materials also tried to enhance and broaden sound absorption spectrum through graded or multilayer structures [27–29]. These studies indicate that an even higher absorption can be achieved with an alternating sequence of porous layers with high and low airflow resistivity rather than a monotonic grading. Various numerical techniques, such as the transfer matrix method (TMM) [26,29,30], Peano series [30,31], and wave-splitting techniques with transfer Green's functions [27,30], have been employed to model the acoustic properties of such graded or multilayer porous materials.

In contrast to other geometries employed in periodic porous materials, triply periodic minimal surfaces (TPMS) exhibit distinctive characteristics. They are generated by mathematical functions with adjustable parameters, enabling precise control and easy optimization of porosity or periodicity at each position within the structures [32]. Unlike strut-based lattice structures, TPMS structures have smooth surfaces, reducing stress concentrations and thereby enhancing mechanical properties [33]. Moreover, the interconnected pores of TPMS structures result in high surface-area-to-volume ratios [34], which is beneficial for sound absorption. Such open-pore structures are suitable for additive manufacturing methods like powder- and resin-based techniques because their design allows for the removal of excess material from the void spaces. These unique attributes make TPMS particularly attractive for functional applications, for instance, bone implants [35], heat sinks [36], chemical microreactors [37], and acoustic absorbers [9].

The mechanical, thermal and mass transfer performance of TPMS structures have been extensively researched in the recent years [34]. Nevertheless, the potential of TPMS structures as sound absorbers remains to be explored. Early investigations into TPMS sound absorbers primarily focused on impedance tube measurements of 3D printed samples [9,12]. Our recent study computationally characterized acoustic properties of TPMS structures based on their unit cell geometry using a bottom-up approach [38]. However, the optimization of TPMS porous structures for broadband acoustic absorption has not been researched. The aim of this paper is to use the highly tunable TPMS geometry as a basis for the optimization of graded porous structures, in order to reveal the relationship between the geometry parameters of the unit cell, porosity-grading profile and the sound absorption spectrum. The validity of the optimization is confirmed through impedance tube measurements of 3D printed samples.

The paper is structured as follows: Section 2 provides an overview of the design and analysis methods for TPMS absorbers. Section 3 describes the modeling methods and presents the results of the parametric study for uniform TPMS. Section 4 focuses on the modeling and optimization of graded TPMS structures, including the optimization results. Section 5 presents and discusses experimental validation results. Finally, Section 6 summarizes the key findings of the study.

2. Overview of design and analysis methods

Fig. 1 illustrates the schematic representation of our work on optimizing the porosity profile of triply periodic minimal surface (TPMS) lattices. TPMS unit cells can have various forms, such as primitive, diamond, gyroid [32,34]. In this work, we employ the primitive-type cell, which is an isotropic unit cell with cubic symmetry. The primitive type surface can be mathematically described by a level-set function $\varphi_P(x, y, z)$ [32]:

$$\varphi_P(x, y, z) = \cos(\frac{2\pi}{d}x) + \cos(\frac{2\pi}{d}y) + \cos(\frac{2\pi}{d}z) = t(x, y, z), \quad (1)$$

where d is the period in the x-, y-, z-directions in Cartesian coordinates and is equal to the unit cell size. t on the right-hand side is the isovalue, which determines the thickness of the solid frames of TPMS structures. As shown in Fig. 1(a), at an isovalue of $t = 0$, the formula generates an isosurface that evenly divides the entire space into two equal volumes. When $t \neq 0$, the resulting isosurface is displaced inward or outward from the zero-isovalue surface. By establishing the inequality $-t \leq \varphi_p(x, y, z) \leq t$ (for $t > 0$), the region between surfaces with isovalues t and $-t$ is defined as a solid, forming what is known as a sheet lattice [39]. Thus, by tuning the value of t, the porosity of TPMS structures ϕ, defined as the ratio of the volume of air (V_a) to the total volume of the unit cell (V_t), i.e., $\phi = V_a/V_t$, can be controlled. The relationship between the isovalue t and the porosity ϕ is shown in Fig. 1(b), and Fig. 1(c) illustrates the change in shapes of a TPMS unit cell for different porosity values of 50%, 70%, and 90%. Fig. 1(d) shows the acoustic particle velocity and acoustic temperature in the fluid domain of a TPMS cell. It can be seen that the acoustic particle velocity and acoustic temperature tend to decrease significantly near the fluid-solid boundary of TPMS. Additionally, the particle velocity gradient becomes steeper within narrow constrictions of the TPMS geometry. These boundary layer effects cause viscous and thermal dissipation, which are critical mechanisms for acoustic absorption in porous materials.

A TPMS lattice structure with a uniform porosity ϕ and a layer thickness L can be modeled as a homogeneous equivalent acoustic medium of which wave propagation characteristics are governed by its effective density ρ_e and effective bulk modulus K_e, calculated with the JCAL model, as shown in Fig. 1(f). Although the sound absorption performance of a TPMS structure with a uniform porosity is considerably good as depicted in Fig. 1(e), the broadband absorption can be further improved by the grading the porosity profile while maintaining the same thickness. Fig. 1(g) illustrates the graded TPMS case, where the porosity ϕ (range 50% - 90%) is varied along the thickness direction z of the TPMS structure. The continuously graded structure can be discretized as multilayers, where each stacked layer with thickness ΔL can be modeled as an equivalent acoustic medium with effective properties determined by its average porosity ϕ_i. Under plane wave incidence, acoustic properties of this multilayer system can be modeled with the transfer matrix method (TMM). This modeling approach allows for the optimization of the TPMS lattices for desired acoustic absorption simply by adjusting the porosity of each layer. The acoustical modeling and optimization methods will be presented in the following sections.

3. Characterization and parametric study of uniform TPMS structures

In the subsection 3.1, the method to characterize uniform porosity TPMS structures is introduced. Subsequently, the results of a parametric study conducted for uniform TPMS structures with different geometric parameters are presented in the subsection 3.2.

3.1. Equivalent fluid modeling

The solid frame of a sound-absorbing porous material is often assumed to be rigid, resulting in the material being modeled as an equivalent fluid medium [19]. Consequently, the macroscopic characterization of the acoustic properties of the porous material involves determining an effective density, $\rho_e(\omega)$, which accounts for inertial and viscous dissipation, and an effective bulk modulus, $K_e(\omega)$, which accounts for thermal dissipation [19]. In this work, we employ the Johnson-Champoux-Allard-Lafarge (JCAL) model [21–23] to model the TPMS porous structure as a homogeneous medium with effective acoustic properties. The JCAL model is one of most widely used semi-phenomenological models and can be applied to open-cell porous structures with non-uniform pores without abrupt cross-sectional change. The JCAL model requires six transport parameters to calculate the effective properties: the porosity ϕ, the high-frequency limit of the tortuosity a_∞, the static viscous

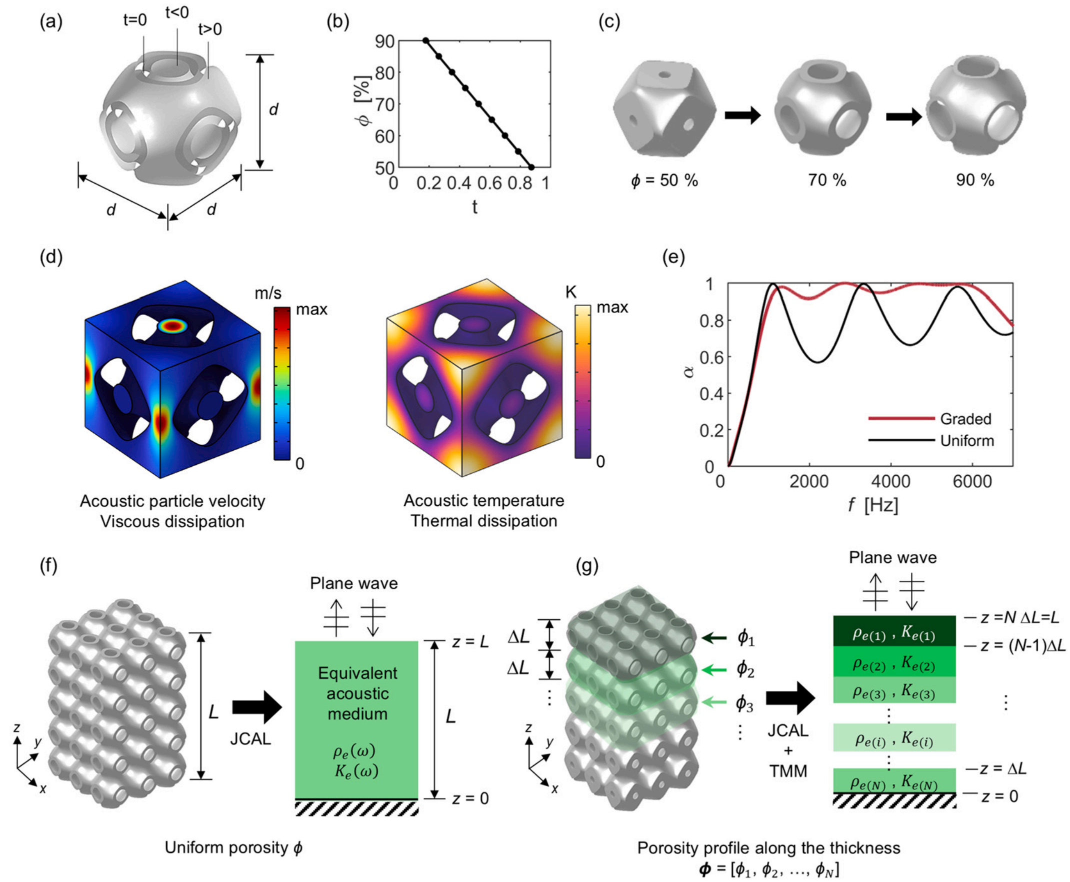

Fig. 1. (a) Geometry of a triply periodic minimal surface (TPMS) unit cell with a period d and isovalue t. (b) Porosity ϕ of a sheet TPMS unit cell as a function of the isovalue t. (c) Shapes of sheet TPMS unit cells for different porosity values. (d) Viscous and thermal dissipation in TPMS unit cell. (e) Comparison of sound absorption coefficients between TPMS absorbers with uniform porosity 69.04% (black line) and those with a graded porosity profile along the thickness (red line). The two configurations (uniform and graded porosities) have the same layer thickness. (f) TPMS absorber with uniform porosity and its equivalent acoustic model. (g) TPMS absorber with a graded porosity profile along the thickness and its equivalent acoustic model.

Table 1
The properties of air at 20 °C.

Fluid properties	Value
Density ρ_0	$1.2\,\mathrm{kg/m^3}$
Dynamic viscosity η	$1.82\times10^{-5}\,\mathrm{N\cdot s/m^2}$
Thermal conductivity κ	$2.6\times10^{-2}\,\mathrm{W/(m\cdot K)}$
Specific heat capacity C_p	$1006\,\mathrm{J/(kg\cdot K)}$
Atmospheric pressure P_0	$101320\,\mathrm{Pa}$
Specific heat ratio γ	1.4
Speed of sound c_0	$343\,\mathrm{m/s}$

permeability k_0, the static thermal permeability k_0', the viscous characteristic length Λ, and the thermal characteristic length Λ'. The effective density $\rho_e(\omega)$ and bulk modulus $K_e(\omega)$ can be computed using the following expressions:

$$\rho_e(\omega) = \frac{\rho_0\alpha_\infty}{\phi}\left[1 + \frac{\eta\phi}{j\omega\rho_0 k_0\alpha_\infty}\sqrt{1 + j\frac{4\rho_0\omega k_0^2\alpha_\infty^2}{\eta\phi^2\Lambda^2}}\right], \tag{2}$$

$$K_e(\omega) = \frac{\gamma P_0/\phi}{\gamma - (\gamma-1)\left[1 - j\frac{\phi\kappa}{k_0' C_p\rho_0\omega}\sqrt{1 + j\frac{4k_0'^2 C_p\rho_0\omega}{\kappa\Lambda'^2\phi^2}}\right]^{-1}}, \tag{3}$$

where ω denotes the angular frequency, ρ_0 the density of air, η the dynamic viscosity, γ the specific heat ratio, P_0 the atmospheric pressure, C_p the specific heat capacity, and κ the thermal conductivity. The values for properties of air are listed in Table 1.

The JCAL parameters can be obtained through numerical methods, such as finite element simulations [4,6,20]. We used COMSOL Multiphysics 6.2 [40] to calculate three static boundary value problems within the fluid (air) domain of a TPMS unit cell to obtain these parameters. These boundary value problems include the Stokes' flow problem (for the calculation of k_0), the electric conduction problem (a_∞ and Λ), and the Poisson's problem (k_0'). ϕ and Λ' are directly calculated from the TPMS geometry. The theory and COMSOL implementation details can be found in the work by Zieliński et al. [20].

As demonstrated in previous studies [4,27,29], JCAL parameters can also be inversely calculated using impedance tube measurements to incorporate the manufacturing effects such as surface roughness and micro-porosity. However, as pointed out by Refs. [8,27], micro-geometric defects are process- and device-dependent, therefore experimental JCAL parameters have high uncertainty. For this reason, we opted to calculate the JCAL parameters numerically rather than using an experimental characterization method. These numerically calculated parameters can serve as a reference for future experimental studies.

In our previous study [38], we presented the numerical calculation results of the six transport parameters of primitive-type TPMS lattices with three different unit cell sizes (d = 0.5 mm, 1 mm, 2 mm) and 9 different porosities ϕ (50%-90%, every 5%). The JCAL parameters (k_0, k_0', Λ, Λ', a_∞) are normalized to the unit cell size d, specifically, the viscous and thermal permeabilities k_0 and k_0' (with unit mm^2) are divided by the square of the unit cell size d^2, while the viscous and thermal characteristic lengths Λ and Λ' (with unit mm) are divided by the unit cell size d. The high frequency limit of the tortuosity a_∞ is an in-

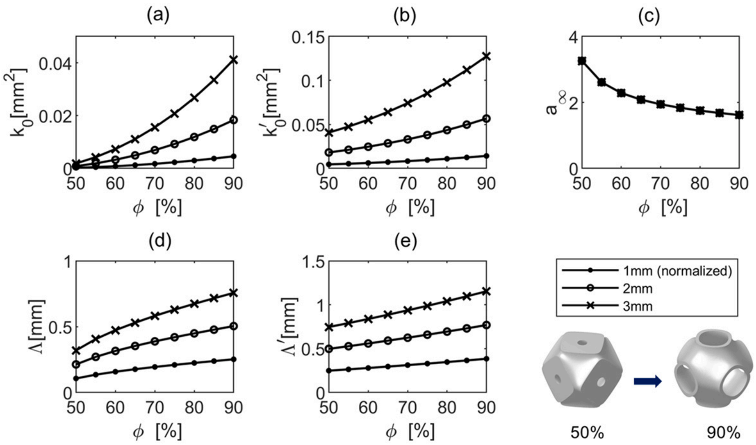

Fig. 2. JCAL parameters of TPMS with the unit cell size $d = 1$ mm, 2 mm, and 3 mm are plotted as a function of the porosity ϕ of the TPMS unit cell. (a) Static viscous permeability k_0, (b) static thermal permeability k_0', (c) high-frequency limit of the tortuosity a_∞, (d) viscous characteristic length Λ, and (e) thermal characteristic length Λ'. Note that the normalized values are the same as those for $d = 1$ mm, without dimensions.

herently dimensionless parameter, thus is not normalized. It was found that, after normalization, JCAL parameters become identical for TPMS with different unit cell sizes. Normalized parameters are independent of the absolute size of the unit cell and depend only on porosity ϕ. Fig. 2 shows the relationship between JCAL parameters (unit cell size $d = 1$ mm, 2 mm, 3 mm) and the porosity. When JCAL parameters are normalized to the corresponding unit cell sizes, they yield the same values as the JCAL parameters for $d = 1$ mm. The JCAL parameters increase monotonically with porosity ϕ, except for the high-frequency limit of tortuosity a_∞, which decreases monotonically with porosity. It is worth highlighting that, based on this finding, (i) it is possible to obtain the JCAL parameters for TPMS lattices of any size by performing simulations with cells of just one size, and (ii) due to their monotonous increase or decrease, the parameters for intermediate porosity values can be easily obtained through interpolation and subsequently used in an optimization process.

3.2. Parametric study of uniform TPMS structures

To investigate the influence of geometric parameters on the sound absorption, we conducted parametric studies by changing the porosity ϕ, the unit cell size d, and the total thickness L of the TPMS structure. By using Eqs. (2) and (3), the wavenumber k and the characteristic impedance z_c of the equivalent fluid medium can be determined by

$$k(\omega) = \omega\sqrt{\frac{\rho_e(\omega)}{K_e(\omega)}}, \tag{4}$$

$$z_c(\omega) = \sqrt{\rho_e(\omega)K_e(\omega)}. \tag{5}$$

Then, for normally incident plane waves, the surface impedance Z_s at $z = L$ is calculated as

$$Z_s(\omega) = -\mathrm{j}z_c(\omega)\cot(k(\omega)L). \tag{6}$$

With the surface impedance Z_s, we can subsequently deduce the normal-incidence reflection coefficient R and the absorption coefficient α as follows:

$$R(\omega) = \frac{Z_s(\omega) - \rho_0 c_0}{Z_s(\omega) + \rho_0 c_0}, \tag{7}$$

$$\alpha(\omega) = 1 - |R(\omega)|^2. \tag{8}$$

Figs. 3(a), 3(b), and 3(c) show the reflection coefficients in the complex frequency plane with respect to the geometric parameters: porosity ϕ, unit cell size d, and TPMS lattice structure thickness L, respectively. The reflection coefficients are plotted on a logarithmic scale as $10\log_{10}(|R|^2)$, with the complex frequency $f = f_r + \mathrm{j}f_i$ as the input, where the subscripts r and i denote the real and imaginary part, respectively. The parameters used for the base figure of the reflection coefficients throughout Figs. 3(a), 3(b), and 3(c) are $\phi = 70\%$, $d = 1$ mm, and $L = 50$ mm. Below the complex frequency plane graphs, the corresponding absorption coefficients are presented in Figs. 3(d), 3(e), and 3(f).

The complex frequency plane analysis [41,42] is an effective method for understanding the sound absorption mechanism. The reflection coefficients have pairs of poles and zeros, which are identified as dark green (poles) and brown (zeros) areas in the graphs. In the absence of losses, the poles and zeros are complex conjugate: poles have a negative imaginary part and zeros have a positive imaginary part. The zeros in the graphs are associated to the so-called quarter-wavelength resonances, where odd multiples of quarter-wavelength match the thickness of an absorbing layer. When losses are introduced to the system, the pole-zero pairs are shifted downwards in the complex frequency plane. Ultimately, when the zeros are located on the real axis ($f_i = 0$, indicated as dashed black line on the graphs), total absorption $\alpha = 1$ occurs. This phenomenon is known as impedance matching or the critical coupling condition. Thus, by examining the location of zeros in the complex plane, we can easily determine if the system is underdamped (zeros located above the real axis) or overdamped (below the real axis). For instance, for the base configuration ($\phi = 70\%$, $d = 1$ mm, and $L = 50$ mm) used in the complex frequency plane analysis in Figs. 3(a), 3(b), and 3(c), the first resonance is slightly underdamped, the second resonance leads to almost perfect absorption, and the third resonance is slightly overdamped. This is translated into the absorption coefficients (see the absorption coefficient graphs Figs. 3(d)-(f), black line) as the first absorption peak value 0.9929, the second 0.9981, and the third peak 0.9848.

Figs. 3(a) and 3(d) show the results when the porosity ϕ is varied from 50% to 90%. The unit cell size d and the porous layer thickness L are fixed to 1 mm and 50 mm, respectively. On the reflection coefficient graph, the trajectories of zeros are plotted according to the change of the porosity. As the porosity decreases, the air passages in the TPMS lattices become narrower, increasing the losses of the system. This causes the zeros of reflection coefficients to shift downwards on the complex plane. Most of the trajectories of zeros cross the real axis when the porosity is approximately 70%, which indicates that approximately 70% of porosity is optimal to get the highest absorption for the considered configuration ($d = 1$ mm and $L = 50$ mm). As the porosity deviates from 70%, the zeros locate further away from the real axis, therefore resulting in lower absorption coefficients compared to the 70% case. Note that the same study can be conducted for larger unit cell sizes. In Section S1 of Supplementary Information, we have include a parameter study for unit cell

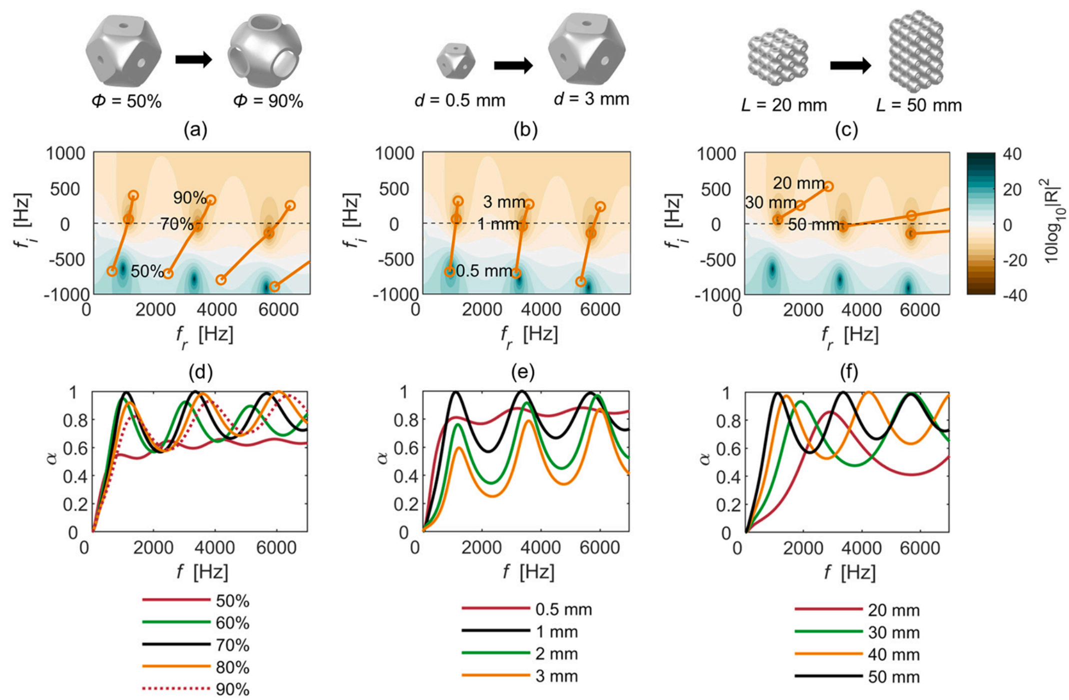

Fig. 3. Reflection coefficients in complex frequency plane of uniform-porosity TPMS structures for varied (a) porosity ϕ, (b) unit cell size d, and (c) thickness L. (d), (e), and (f) show absorption coefficients for each corresponding case (a), (b), and (c). The base figure in (a)-(c) used the parameters $\phi = 70\%$, $d = 1$ mm, and $L = 50$ mm. The open circles mark the trajectories of zeros.

sizes of $d = 3$ mm, 5 mm, and 7 mm. Generally, increasing the unit cell size leads to lower optimal porosity values.

Additionally, as the porosity decreases, the zeros shift to lower frequencies and become more closely spaced horizontally. This phenomenon originates from the increase in the high-frequency limit of the tortuosity a_∞ with the decrease of porosity (see Fig. 2(c)). Tortuosity is a parameter that describes the complexity of the wave passage through the material. A tortuosity value of 1 indicates a straight path, whereas a tortuosity value of 2 means that the effective wave propagation path is twice the length of the straight path. Consequently, the frequencies corresponding to the quarter-wavelength resonances shift downwards with the increase in tortuosity. For instance, if we compare the 90% porosity and 50% porosity cases, the first resonance frequency of the 90% porosity case ($a_\infty = 1.6172$) is 1276 Hz, whereas that of the 50% porosity ($a_\infty = 3.2598$) case is 582 Hz. The ratio between the tortuosities and the first resonance frequencies are similar, demonstrating the direct relationship between increased tortuosity and lower resonance frequencies.

In Figs. 3(b) and 3(e), the unit cell size d is changed from 0.5 mm to 3 mm, while the porosity ϕ and the porous layer thickness L are fixed to 70% and 50 mm, respectively. From Fig. 3(b) we can see that the decreasing unit cell size shifts the zeros mainly vertically, which means that the decrease of the unit cell size mainly contributes to the increase of the loss of the system. When the porosity is fixed, the decrease of the unit cell size results in the decrease of the size of the air passage in the TPMS cells, which in turn increases the loss of the system similar to the case of Figs. 3(a) and 3(d). However, as the porosity is fixed, the tortuosity a_∞ of the TPMS cell does not change. Therefore a relatively smaller horizontal shift is observed compared to the Figs. 3(a) and 3(d) case. Reducing the unit cell size from 3 mm enhances sound absorption, reaching highest absorption at quarter-wavelength resonances when the unit cell size is 1 mm; however, further reduction introduces excess losses, thereby diminishing absorption peaks.

In Figs. 3(c) and 3(f), the thickness of the TPMS layer L is changed from 20 mm to 50 mm, while the porosity ϕ and the unit cell size d are fixed to 70% and 1 mm, respectively. From Fig. 3(c) we can see that changing the thickness mainly leads to the horizontal shift of the zeros. When the thickness is increased, the location of zeros are closer to each other, resulting in more quarter wavelength resonance peaks in the shown frequency range. The locations of zeros also move down slightly when the thickness is increased, meaning that addition of more TPMS cells increases the losses of the system. The system reaches perfect absorption at first resonance peak when the thickness is about 50 mm.

We can conclude from the parametric study that the quarter-wavelength resonance frequencies and the corresponding absorption coefficients of a uniform-porosity TPMS structure can be effectively tuned by adjusting its geometric parameters. However, the absorption peak frequencies lie far apart from each other due to the strong dependence of the absorption mechanism on quarter-wavelength resonances. This leads to troughs between the peaks, making it unfeasible to achieve a high and flat absorption curve across a broad frequency range with uniform-porosity structures. Hence, in the next section, we introduce the porosity grading along the thickness and optimize the porosity profile in order to improve broadband absorption.

4. Optimization of TPMS structures

In this section, we first introduce the transfer matrix method used to model the graded TPMS structure in the subsection 4.1. Then, the optimization problem is formulated in the subsection 4.2. Finally, the optimization results are presented and discussed in the subsection 4.3.

4.1. Transfer matrix method

As introduced in Section 2, a TPMS structure with a graded porosity profile can be modeled as multiple equivalent fluid layers, whose properties are determined by their porosity (see Fig. 1(f)). In this work, the TPMS structure of total thickness L is divided into N layers of equal thickness ΔL. Following the equivalent fluid modeling method introduced in Section 3.1, the effective mass density $\rho_{e(i)}(\omega)$ and effective bulk modulus $K_{e(i)}(\omega)$ of the i^{th} layer ($i = 1, 2, ..., N$) can be determined by using the JCAL transport parameters obtained from the porosity ϕ_i, as presented in Eqs. (2) and (3). Subsequently, the wavenumber $k_i(\omega)$ and the characteristic impedance $z_i(\omega)$ of the i^{th} layer can be obtained by using Eqs. (4) and (5).

The relationship between the sound pressure and velocity of neighboring layers can be described using the transfer matrix method (TMM) [19]. Each layer i is represented by a 2×2 matrix $\mathbf{TM}^{(i)}$ expressed in terms of the thickness of the layer ΔL, its wave number k_i, and its characteristic impedance z_i:

$$\mathbf{TM}^{(i)} = \begin{bmatrix} \cos\left(k_i(\omega)\Delta L\right) & \mathrm{j}z_i(\omega)\sin\left(k_i(\omega)\Delta L\right) \\ \frac{\mathrm{j}\sin\left(k_i(\omega)\Delta L\right)}{z_i(\omega)} & \cos\left(k_i(\omega)\Delta L\right) \end{bmatrix}. \tag{9}$$

The total transfer matrix $\mathbf{TM}$ of the graded TPMS is then determined by multiplying the transfer matrices of all individual layers:

$$\mathbf{TM} = \prod_{i=1}^{N} \mathbf{TM}^{(i)}. \tag{10}$$

The surface impedance Z_s of a graded TPMS absorber with a rigid backing can be obtained with the components of the total transfer matrix in Eq. (10):

$$Z_s(\omega) = \frac{\mathrm{TM}_{11}}{\mathrm{TM}_{21}}, \tag{11}$$

where the subscripts of TM denote the matrix components.

Similar to the uniform-porosity case, Eq. (7) and Eq. (8) are applied to calculate the normal incidence reflection and absorption coefficients of graded TPMS structures.

4.2. Formulation of the optimization problem

The aim of this optimization is to find the optimal porosity profile that maximizes the absorption coefficients in the target frequency range 500-6000 Hz. This target range covers the first three reflection coefficient zeros present in the parametric study of a 50 mm-thick TPMS porous layer (Fig. 3). From Eq. (8), the absorption coefficient α is maximized when $|R|^2$ is minimized. Thus, the objective function $J(\boldsymbol{\phi})$ is set as

$$J(\boldsymbol{\phi}) = \min \sum_{f=f_{min}}^{f_{max}} |R(\boldsymbol{\phi}, f)|^2, \tag{12}$$

where $\boldsymbol{\phi}$ is a vector containing the porosity of each discrete layer, $\boldsymbol{\phi} = [\phi_1, \phi_2, ..., \phi_i, ..., \phi_N]$, $\phi_i \in [50\%, 90\%]$, and $R(\boldsymbol{\phi}, f)$ is the reflection coefficient with respect to the porosity profile $\boldsymbol{\phi}$ and the frequency f. f_{min} and f_{max} are the minimum and maximum frequencies of the target frequency range. The range of ϕ_i is determined by the geometric limit of a primitive TPMS sheet lattice cell: below 50%, self-intersections of the surfaces occur, while above 90%, the walls become excessively thin. A unit cell size $d = 1$ mm is used. Based on our finding in Ref. [38], we chose a layer thickness $\Delta L = 2$ mm for the optimization problems. The layer thickness $\Delta L = 2$ mm provided the best agreement between the TMM discrete modelling approach and full simulations using COMSOL Multiphysics. This choice ensures accurate determination of the acoustic properties while minimizing computational costs.

We use the `fmincon()` [43] and `globalsearch()` functions [44] from the MATLAB nonlinear optimization toolbox to solve this constrained optimization problem. These two functions are designed to be used together to search for the global optimum. Following the framework described in the work of Ugray et al. [44], the global search approach identifies the global optimum by generating multiple starting points and obtaining local optima within their respective basins of attraction using a gradient-based solver like `fmincon()`. The function `fmincon()` is a gradient-based optimization method intended for problems where both the objective and constraint functions are continuous and possess continuous first derivatives [43].

Table 2
The average absorption coefficients $\bar{\alpha}$ in the target frequency range 500-6000 Hz.

Profile type	$L = 50$ mm	$L = 30$ mm
Graded	$\bar{\alpha} = 0.9415$	$\bar{\alpha} = 0.8577$
Uniform	$\bar{\alpha} = 0.7909$	$\bar{\alpha} = 0.6978$
Linear	$\bar{\alpha} = 0.8594$	$\bar{\alpha} = 0.6928$

The global search method employed in this study combines the efficiency of gradient-based local solvers with a systematic exploration of the design space. This hybrid strategy achieves computational efficiency superior to conventional global optimization methods such as genetic algorithms [45] and particle swarm optimization [46], while simultaneously mitigating two key drawbacks of purely gradient-based techniques: (1) susceptibility to convergence at local minima and (2) heavy reliance on initial point selection [47], making it particularly suitable for our optimization problems.

The initial value of the optimization is a linearly decreasing porosity profile from 90% (top) to 50% (bottom). However, note that experiments using different initial porosity profiles have shown that the optimization result does not depend on the initial porosity profile. Furthermore, increasing the number of starting points in `globalsearch()` reduces the randomness of the algorithm and enhances the likelihood of converging to the global optimum [44]. In our work, we use 1000 starting points to ensure a robust and converged solution and repeated experiments yield consistent optimization results.

4.3. Optimization results and discussion

The optimization results for a layer thickness $L = 50$ mm are shown in Fig. 4. Fig. 4(b) displays three types of porosity profiles of the TPMS structures: graded (red line), uniform (black line), and linear (black dotted line). The 'graded' profile is the optimal solution, while the 'linear' profile is the initial porosity profile used for the optimization. To demonstrate the benefit of porosity grading, optimization was also conducted for the case of uniform-porosity TPMS structures. The 'uniform' porosity indicates the optimal solution for this uniform-porosity optimization. The optimal solution for the uniform-porosity optimization is $\phi = 69.04\%$, as predicted in the parametric study presented in Section 3.2, where a porosity approximately 70% was found to be optimal for achieving the highest absorption for TPMS structures with a unit cell size $d = 1$ mm and a thickness $L = 50$ mm. The optimal graded solution ('graded'), however, shows a profile with porosity jumping from the lowest to the highest values.

Fig. 4(d) shows the absorption coefficients of the three cases, i.e., graded, uniform, and linear porosity profiles. The absorption coefficient of the uniform-porosity TPMS structure exhibits three distinctive absorption peaks, originating from the quarter-wavelength resonances as explained in Section 3.2. Compared to the uniform-porosity case, the linear-gradient profile increases absorption in the frequencies between the resonance frequencies; however, it does not enhance the absorption drastically. On the other hand, the graded profile with jumping porosity values significantly enhances the absorption compared to the other two cases. The average absorption coefficients $\bar{\alpha}$ of the three cases in the target frequency range 500-6000 Hz are listed in Table 2. The optimal graded absorber has the highest $\bar{\alpha}$ among the three cases.

A noticeable difference between the graded case and the other two cases is that the absorption between the resonance peaks is increased by the presence of a new absorption peak. Figs. 4(e) and 4(f) show the reflection coefficients of the uniform and graded porosity cases in the complex frequency plane. While the uniform porosity case has three zeros close to the real axis within the target frequency range, the graded case has four zeros. It indicates that the optimal porosity profile generates more resonances within the target frequency range closer to the critical coupling condition to maximize the absorption. This result aligns

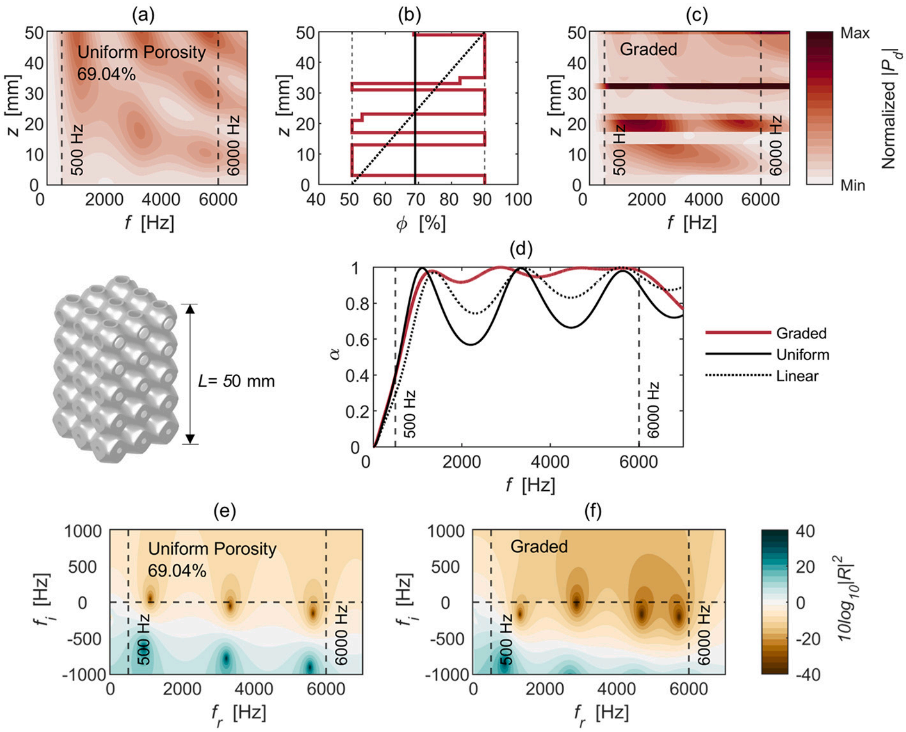

Fig. 4. Broadband optimization with a thickness of $L = 50$ mm. (a) Power dissipation density inside the uniform-porosity (69.04%) TPMS structure. (b) Porosity values of the graded (optimal solution), uniform, and linear-gradient profiles. (c) Power dissipation density inside the optimally graded TPMS structure. (d) The absorption coefficients of TPMS structures with graded, uniform, and linear porosity profiles presented in (b). (e) and (f) present reflection coefficients in the complex frequency plane for uniform and graded porosity cases, respectively.

with the findings of Boulvert et al. [27] and Costa-Baptista et al. [29], who also obtained an optimal profile as an alternating distribution of contrasting porosity (or infill factor) values from the optimization of the size distribution of orthogonal rods for broadband sound absorption.

To investigate the relationship between the porosity profile $\boldsymbol{\phi}$ and the sound dissipation inside TPMS structures, we visualize the sound power dissipation density P_d with respect to the z position and the frequency f. The sound power dissipation density P_d can be calculated with the following equation [48]:

$$P_d = 2\omega \left\{ \frac{1}{2}\mathrm{Im}(\rho_e(\omega))|v|^2 + \frac{1}{2}\mathrm{Im}(\frac{1}{K_e(\omega)})|p|^2 \right\}, \tag{13}$$

where p and v are the acoustic pressure and particle velocity derived from the TMM calculation, and Im() indicates the imaginary part of a complex number. Note that the value of the acoustic power dissipation density P_d in Eq. (13) is negative because the imaginary part of the effective density ρ_e and the effective bulk modulus K_e are negative in sound-dissipating porous materials. The value in all dissipation density graphs is made positive and normalized by the incident sound power. Summing the normalized power dissipation density throughout the porous layer for each frequency gives a value equal to the absorption coefficient. The visualization of the power dissipation density of the uniform and graded TPMS structures are shown in Figs. 4(a) and 4(c), respectively. In the uniform-porosity case (Fig. 4(a)), the dissipation is higher around the quarter-wavelength resonance frequencies of the TPMS structure. While the dissipation around the first resonance frequency occurs most near the surface of the porous layer ($z = 50$ mm), at higher resonance frequencies, the inner part of the porous layer also participates in dissipating sound energy. However, in the graded-porosity case (Fig. 4(c)), the dissipation occurs predominantly in the region of low porosity for a broad frequency range.

To further understand how the optimal profile is determined, optimization studies were conducted to maximize the absorption coefficient at a single target frequency f_0. The same unit cell size of 1 mm and the layer thickness of 50 mm were used. We conducted the single-frequency optimization for three frequencies: (i) $f_0 = 700$ Hz, a frequency below the first absorption peak in the reference uniform-porosity case, (ii) $f_0 = 2000$ Hz, between the first and second absorption peaks, and (iii) $f_0 = 5000$ Hz, between the second and third absorption peaks. Fig. 5(a) shows the optimal porosity profiles obtained from three single-frequency optimization studies. Figs. 5(b), 5(c), and 5(d) visualize the power dissipation density P_d inside optimal graded TPMS structures for single-frequency optimization cases. Figs. 5(e), 5(f), and 5(g) show absorption coefficients of the three optimization cases. The optimized absorption coefficients of these cases are compared with the absorption coefficients of the uniform-porosity optimization (optimal porosity 69.04%) for broadband sound absorption presented earlier. Figs. 5(h), 5(i), and 5(j) show reflection coefficients in the complex frequency plane of the three optimization cases.

For the target frequency $f_0 = 700$ Hz, the low-porosity region locates near the top surface of the porous layer (higher z coordinate), while the porosity in the lower part of the porous layer reaches the upper bound of the porosity value 90%. As shown in Section 3.2, decreasing porosity brings two effects: an increase in loss and an increase in tortuosity. In the $f_0 = 700$ Hz optimization case, the optimization produced a solution that lowers the first resonance frequency by increasing the tortuosity of the top layers. A similar approach is observed in the work of Carbajo et al. [49], where they investigated the influence of the tortuosity of perforated panels. The low porosity values also increase the loss, leading to strong dissipation in the low-porosity region. As observed in Figs. 3(a) and 3(d), an excessive increase of loss can overdampen the system, resulting in low absorption. Thus, the optimization pushed the porosities in the lower layers to the opposite high values to balance the effects. However, there is still excess loss for frequencies higher than f_0 (see Fig. 5(h)), causing lower absorption at these frequencies.

For the target frequency $f_0 = 2000$ Hz, the optimization produces two distinct low-porosity (high-dissipation) zones: one near the surface of the porous layer and the other around $z = $ 10-20 mm, as shown in

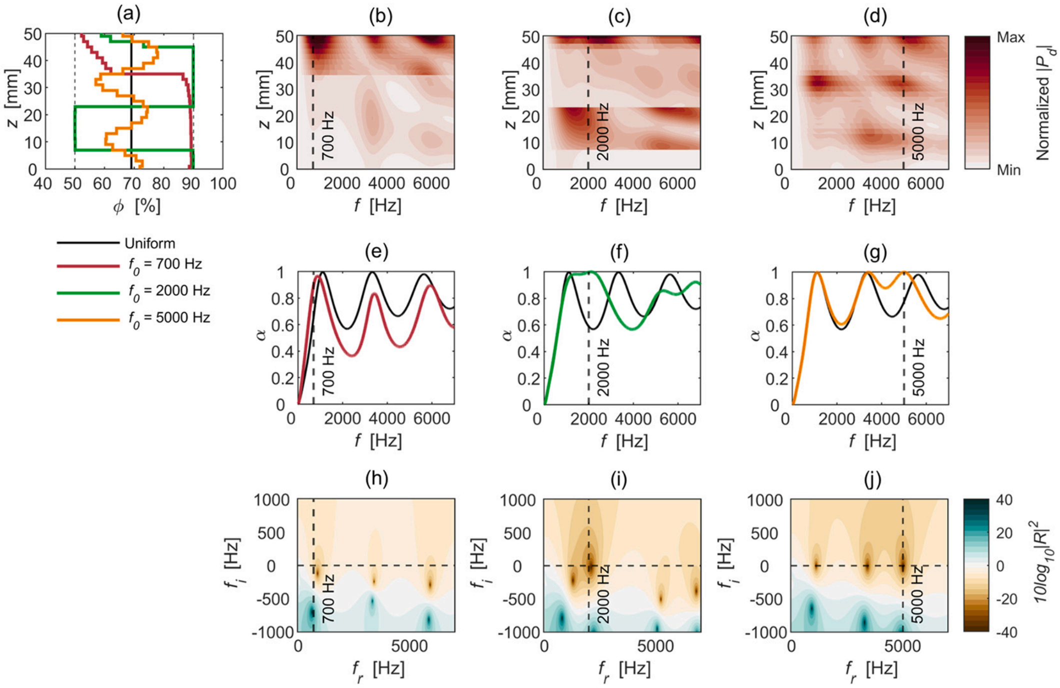

Fig. 5. Results of the single-frequency optimization. (a) Optimized porosity profiles for the target frequencies f_0 = 700 Hz, 2000 Hz, and 5000 Hz, and uniform porosity profile (69.04%). (b), (c), and (d) show the power dissipation densities inside the optimally graded TPMS structure for f_0 = 700 Hz, 2000 Hz, and 5000 Hz, respectively. (e), (f), and (g) show the absorption coefficients of the optimally graded TPMS structure for three target frequencies, respectively. (h), (i), and (j) show the reflection coefficients in the complex frequency plane of the optimally graded TPMS structure for three target frequencies, respectively.

Figs. 5(a) and 5(c). These low-porosity regions roughly correspond to areas of high dissipation around the second absorption peak (around 3000 Hz) in the uniform-porosity case (Fig. 4(a)). With the increased tortuosity induced by these low-porosity regions, the original perfect absorption peak at 3000 Hz is downshifted to 2000 Hz, however, this optimized porosity profile again caused overdamping for higher frequencies (see Figs. 5(f) and 5(i)), similar to the f_0 = 700 Hz case.

For f_0 = 5000 Hz, the optimized porosity profile resembles a sinusoidal shape, with three low-porosity (high-dissipation) regions evenly distributed along the porous layer, as shown in Figs. 5(a) and 5(d). The optimization produces a smoother porosity profile than the previous cases, likely due to the fact that this target frequency only requires slight modification of the original quarter-wavelength resonance of the uniform porosity case. The sinusoidal porosity pattern generally increases the tortuosity, allowing the absorption peak to shift slightly downward while increasing loss in the areas of higher dissipation, particularly around the third quarter-wavelength resonance. This results in enhanced absorption around the target frequency.

The single-frequency optimization further confirms the strong dependence of the optimized porosity profile on the target frequency. In graded TPMS structures, new resonance modes are formed. These resonance modes can be seen as a modulation of the original quarter-wavelength resonance modes observed in uniform-porosity structures. The optimization is able to shift one or multiple quarter-wavelength resonance peaks by strategically placing low-porosity regions near the original high-dissipation areas within the layer that are related to the quarter-wavelength resonances. The porosity profile has a more abrupt jump when a larger modulation is required, for instance in f_0 = 700 Hz, f_0 = 2000 Hz, and broadband optimization cases. It can be also observed that when maximizing the absorption in a certain frequency range, the absorption above the frequency range is usually compromised due to excess losses.

A different porous layer thickness (L = 30 mm) is used in order to investigate the influence of the thickness on the optimized porosity profiles and the absorption coefficients. The optimal graded and uniform profiles as well as the initial linear profile for the optimization are shown in Fig. 6(b). The corresponding absorption coefficients for these three cases are plotted in Fig. 6(d). The power dissipation of the uniform and graded TPMS structures with a thickness of 30 mm are visualized in Figs. 6(a) and 6(c). Figs. 6(e) and 6(f) analyze the reflection coefficients of the uniform and graded cases in the complex frequency plane.

Compared to the 50 mm case, the 30 mm-thick porous layer has a lower optimal uniform-porosity ϕ = 60.15%. As shown in Figs. 3(c) and 3(f), when both the porosity and unit cell size are fixed, a thinner layer has lower loss than a thicker one. To compensate for this reduced loss, the optimal uniform porosity of a 30 mm-thick layer would be lower than that of a 50 mm-thick layer. From Figs. 6(a)-(c), it can be noticed that the number of low porosity and high dissipation regions in the 30 mm-thick case is lower than in the 50 mm-thick case. This results in fewer resonance modes, indicated by the presence of fewer reflection coefficient zeros in the target frequency range, as shown in Figs. 6(e) and 6(f). Furthermore, the first absorption peak frequency is higher compared to the 50 mm case, and far away from the lower bound of the target frequency range (500 Hz). While the optimization algorithm attempts to shift the resonance modes to lower frequencies, the intrinsic limitation imposed by the layer's thickness prevents them from being shifted further downwards. Thus, it is more difficult to achieve a flat absorption curve in the same target frequency range with a thinner TPMS absorber (see Figs. 4(d) and 6(d)).

While the optimization study primarily focused on a unit cell size d = 1 mm with a porosity range of ϕ = [50%, 90%], the same optimization algorithm can be applied for different unit cell sizes and/or different porosity ranges. Optimization results for a larger unit cell size and a narrower porosity range are provided in Sections S2 and S3 of the Supplementary Information, respectively.

5. Experimental validation of TPMS absorbers

In previous sections, a numerical model and an optimization method were developed to explore the sound absorption properties of pure TPMS geometry, and as such, it does not incorporate the effects of manufacturing processes. For experimental validation, we chose the DLP tech-

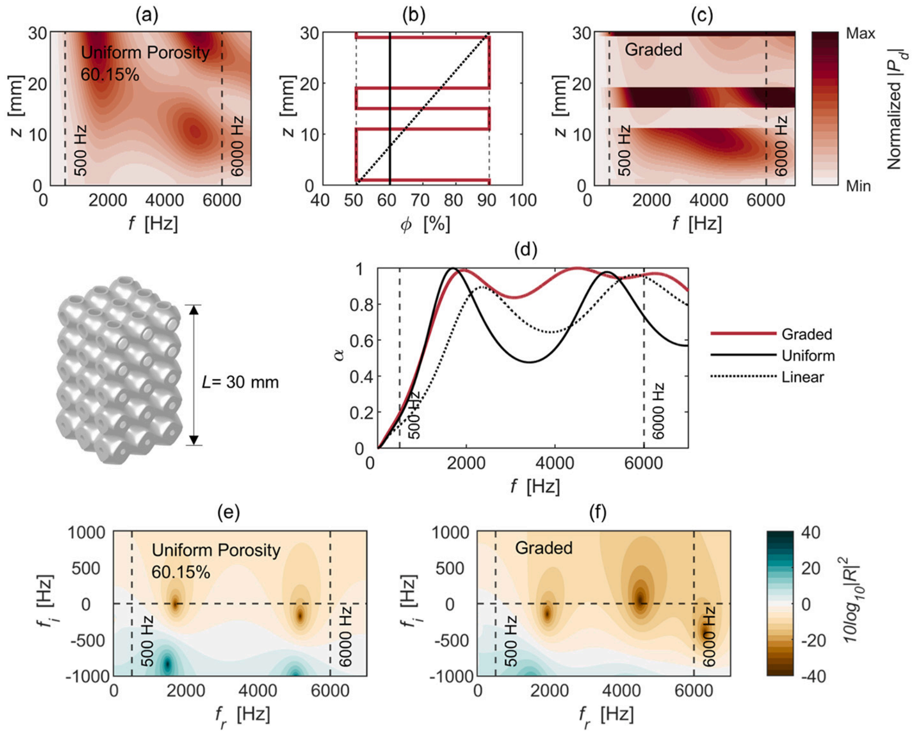

Fig. 6. Broadband optimization with a thickness of $L = 30$ mm. (a) Power dissipation density inside the uniform-porosity (60.15%) TPMS structure. (b) Porosity values of the graded (optimal solution), uniform, and linear-gradient profiles. (c) Power dissipation density inside the optimally graded TPMS structure. (d) The absorption coefficients of TPMS structures with graded, uniform, and linear porosity profiles presented in (b). (e) and (f) present reflection coefficients in the complex frequency plane for uniform and graded porosity cases, respectively.

nique to produce TPMS absorber samples due to its ability to produce smoother surfaces compared to other 3D printing methods [8,10], such as FDM and SLM, to minimize the impact of the printing process.

The DLP printer (MakeX M-One Pro 30) we used to print the samples has an XY resolution of 33 µm and a Z resolution of 5 µm. At this resolution, it is not possible to print a unit cell size smaller than 3 mm. Therefore, for the measurements, we printed TPMS absorbers with 3 mm unit cells. To print a 1 mm unit cell, an XY resolution of around 10 µm would be required. The numerical results for TPMS with 1 mm cells can be validated by measurements of 3D printed samples with 3 mm cells, because the dissipation mechanism of porous materials remains the same across different unit cell sizes.

We manufactured three samples with a thickness of 30 mm and two samples with a thickness of 50 mm. STL models of these designs were created using MSLattice [39]. Fig. 8(a) shows the picture of the manufactured samples. The 30 mm thick samples have porosity profiles that are uniform (Fig. 8(b)), linearly varying (Fig. 8(c)), and optimally graded for broadband absorption in the 2000-5000 Hz range (Fig. 8(d)). The 50 mm thick samples consist of optimal gradation for broadband (2000-5000 Hz) (Fig. 8(e)) and for a single target frequency (2700 Hz) (Fig. 8(f)). These target frequency ranges are selected to shift the absorption peaks in the uniform porosity case, to generate various porosity profiles, and to demonstrate their manufacturability. Discrete profiles in the numerical modeling and the optimization (black lines) were replaced with continuous profiles in the 3D printing (green lines), as shown in Figs. 8(b)-(f).

Based on the two-microphone transfer function method according to ISO 10534-2 [50], the absorption coefficients of the TPMS samples were measured using a 29 mm-diameter B&K Type 4206 impedance tube with a rigid backing configuration, together with a power amplifier (B&K Type 2735) and an analyzer (B&K Type 3160), as shown in Fig. 7. The valid frequency range of the impedance tube is 500 to 6400 Hz.

Figs. 8(g)-(k) show the absorption coefficients obtained through numerical methods (black dashed lines) and measurements (red lines). Generally, the measured absorption coefficients align very well with the numerical results. Fig. 9 shows microscopic images of 3D-printed samples. These images confirm that DLP-printed samples retain well-defined pore morphology and exhibit smooth surfaces, though layer lines remain visible and some stringing occurs as a result of the additive manufacturing process. This inherent surface roughness, originating from the layer-by-layer deposition, contributes to slightly higher experimental sound absorption coefficients compared to idealized numerical predictions. This is consistent with prior studies of 3D-printed porous absorbers [4,6,10,29]. The resonance peaks of 3D-printed samples generally align well with the prediction, despite some shifting in frequency. As discussed in previous sections, absorption spectrums of TPMS absorbers are sensitive to their porosity profiles. Printing intricate porous networks is still challenging due to the limitations in precision of current manufacturing methods. This limits the accurate translation of design porosity profiles into 3D-printed samples, thereby causing the shifting in resonance peaks in the measurement results.

In general, the experimental results confirm the effectiveness of our numerical modeling and optimization approach for graded TPMS porous absorbers, demonstrating their potential in targeted acoustic absorption.

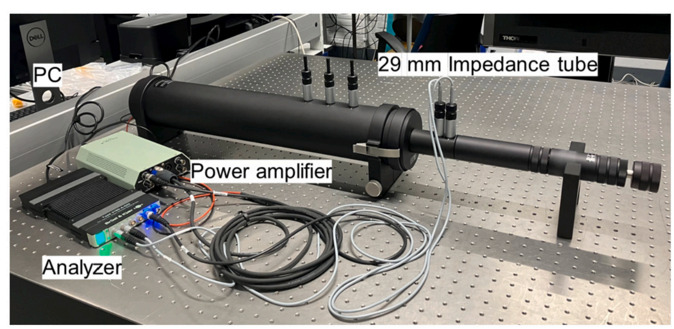

Fig. 7. Impedance tube measurement setup.

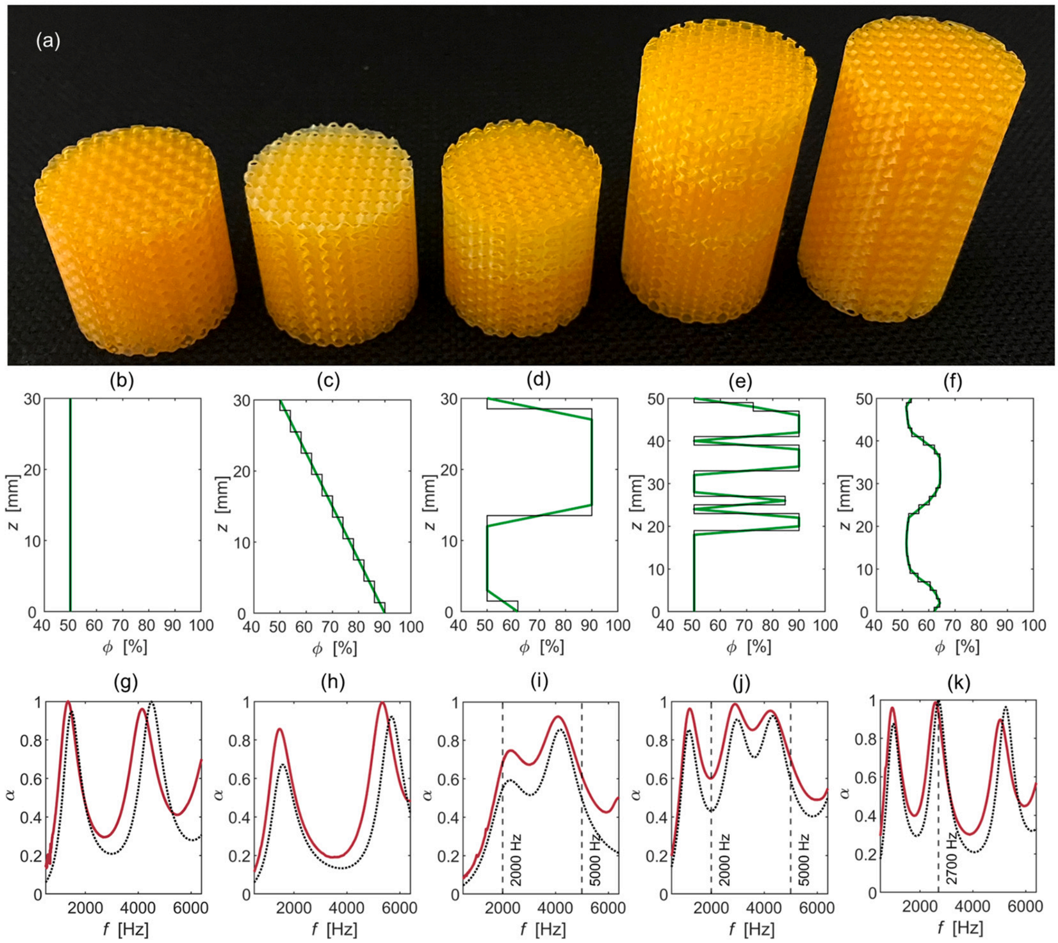

Fig. 8. (a) 3D-printed samples, (b)-(f) associated porosity profiles, and (g)-(k) absorption coefficients: (b)(g) 30 mm thick, uniform porosity 50%; (c)(h) 30 mm thick, linearly varying porosity from 50% to 90%; (d)(i) 30 mm thick, grading optimized for 2000-5000 Hz; (e)(j) 50 mm thick, grading optimized for 2000-5000 Hz; (f)(k) 50 mm thick, grading optimized for 2700 Hz; Green lines in (b)-(f) indicate continuous profiles in 3D printing, black solid lines in (b)-(f) denote discrete profiles in optimizations, red lines in (g)-(k) represent measurement results, and black dashed lines in (g)-(k) correspond to numerical results.

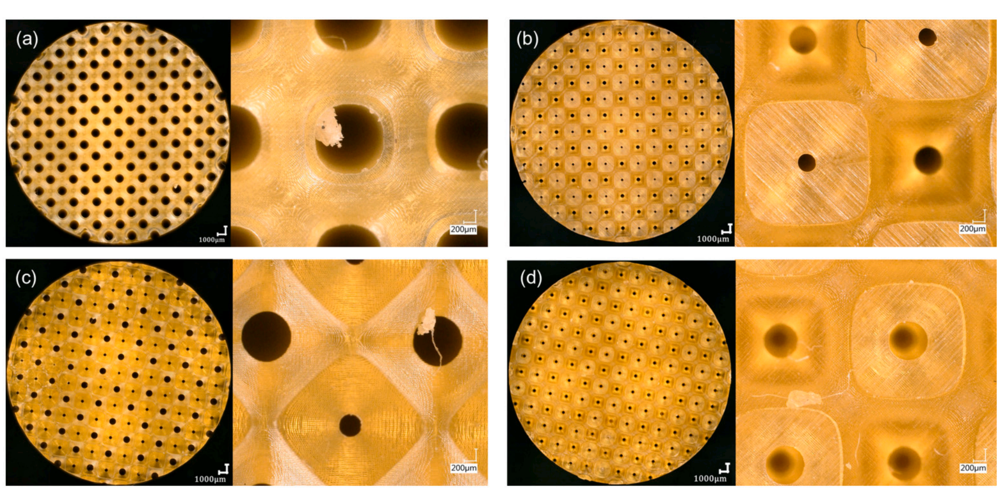

Fig. 9. Microscopic images of 3D-printed samples: (a) the sample in Fig. 8(c), section $z = 0$ mm, (b) the sample in Fig. 8(c), section $z = 30$ mm, (c) the sample in Fig. 8(d), section $z = 0$ mm, (d) the sample in Fig. 8(d), section $z = 30$ mm.

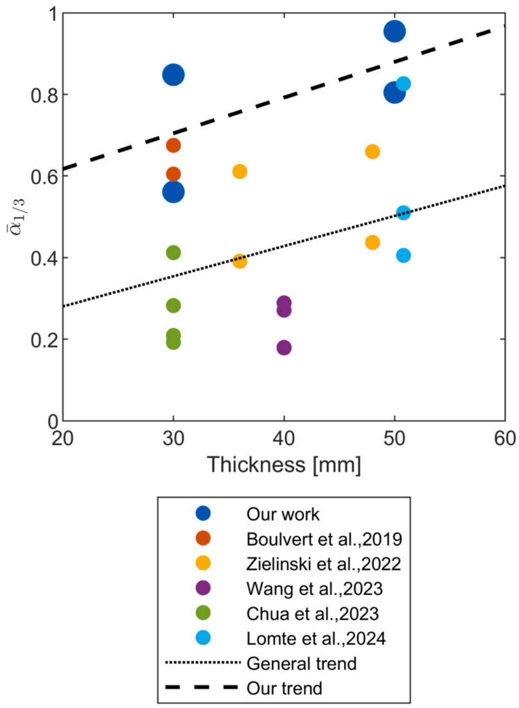

Fig. 10. Comparison of the acoustic performance of the optimized TPMS with other lattice structures in the literature.

6. Comparison of the acoustic performance of the optimized TPMS to other lattice structures in the literature

To compare the acoustic performance of graded TPMS absorbers with various lattice structures reported in the literature, their average sound absorption coefficients $\bar{\alpha}_{1/3}$ were computed across eight one-third octave bands spanning the 1000 Hz to 5000 Hz range, which is a frequency range particularly relevant for the sound absorption properties of acoustic porous materials. We plotted the average absorption coefficients $\bar{\alpha}_{1/3}$ versus thicknesses in Fig. 10 to illustrate the absorption coefficient variation with respect to thickness. Two lines were fitted to the data points from our work (labeled "our trend") and prior studies (labeled "general trend"), respectively, to compare the performance-thickness relationship of TPMS absorbers with that of other lattice structures. It can be seen that the graded TPMS absorbers developed in our work exhibit superior acoustic performance at reduced thicknesses compared to other lattice structures reported in previous studies. Additionally, Table A.3 in Appendix A presents the average sound absorption coefficients $\bar{\alpha}_{1/3}$ of all 3D-printed lattice structures in Fig. 10.

7. Conclusions

In this work, we proposed a design methodology for sound absorbers based on triply periodic minimal surfaces (TPMS) by tuning the porosity distribution along the thickness to achieve broadband sound absorption. To accomplish this, we presented a comprehensive numerical modeling method that combines multiscale homogenization, the Johnson-Champoux-Allard-Lafarge (JCAL) model, and the transfer matrix method to effectively characterize through-thickness graded TPMS porous absorbers. The JCAL parameters for primitive-type sheet TPMS lattices with varying cell sizes and porosities were derived from finite element simulations, forming an interpolative dataset. Using this dataset, we first analyzed the influence of geometric parameters (porosity, unit cell size, and total thickness) on the sound absorption of uniform-porosity TPMS absorbers by mapping the reflection coefficient zeros in the complex frequency plane. The analysis showed that the geometric tunability of TPMS structures allows for the adjustment of viscothermal losses within the porous absorber. However, the use of uniform porosity TPMS did not significantly improve broadband sound absorption performance.

Thus, the proposed numerical model was further employed to optimize the grading of TPMS absorbers using a global search method combined with a local gradient-based solver, aiming to maximize broadband acoustic absorption. To elucidate the relationship between the grading and the absorption coefficient, the energy dissipation within the absorber was visualized by plotting the power dissipation density with respect to the frequency and the position. The results showed that, in graded porous absorbers, power dissipation density is redistributed across the spatial and frequency domains, leading to enhanced broadband absorption when optimally graded. However, modifying the porosity profile alone has limitations in improving low-frequency absorption; this would require adopting other design methodologies, such as those presented in Refs. [15,51–53].

For experimental validation of the proposed approach, we 3D-printed five samples with varying thicknesses and porosity profiles, including the optimally graded ones, and compared the absorption coefficients obtained through numerical methods with those from impedance tube measurements. The numerical and experimental results showed good agreement, except for minor discrepancies, demonstrating the accuracy and effectiveness of the proposed acoustical characterization and optimization methods of TPMS absorbers. The graded TPMS absorbers developed in this work achieve superior sound absorption performance at significantly reduced thicknesses compared to other 3D-printed lattice structures documented in prior studies.

CRediT authorship contribution statement

Xueying Guan: Writing – original draft, Visualization, Validation, Software, Methodology, Investigation, Formal analysis, Data curation, Conceptualization. **Elke Deckers:** Writing – review & editing, Supervision, Methodology. **Hao Dong:** Writing – review & editing, Software, Methodology. **Maarten Hornikx:** Project administration. **Jieun Yang:** Writing – review & editing, Visualization, Supervision, Resources, Project administration, Methodology, Conceptualization.

Declaration of competing interest

The authors declare that they have no known competing financial interests or personal relationships that could have appeared to influence the work reported in this paper.

Acknowledgement

The authors are grateful to Dr. Tomasz G. Zieliński (IPPT PAN) for sharing implementation details of COMSOL simulations. The authors also thank Sifeng He (TU Delft) for his help in capturing microscopic images of 3D-printed samples.

Appendix A. Comparison with other lattice structures in previous studies

Table A.3 contains the averaged absorption coefficients of our optimized TPMS geometries as well as different lattice structures in previous studies shown in Fig. 10.

Appendix B. Supplementary material

Supplementary material related to this article can be found online at https://doi.org/10.1016/j.matdes.2025.113852.

Data availability

Data will be made available upon reasonable request to the corresponding author.

Table A.3
The average absorption coefficients $\bar{\alpha}$ over one-third octave bands from 1000 Hz to 5000 Hz.

Reference	Structure	L [mm]	$\bar{\alpha}_{1/3}$
Our work	Graded TPMS design (500-6000 Hz, 1 mm cell)	50	0.9548
	Graded TPMS design (500-6000 Hz, 1 mm cell)	30	0.8482
	Graded TPMS measured (2000-5000 Hz, 3 mm cell)	50	0.8047
	Graded TPMS measured (2000-5000 Hz, 3 mm cell)	30	0.5611
Boulvert et al. [27]	Graded orthogonal rods (1600-1700 Hz)	30	0.6047
	Graded orthogonal rods (2500-5500 Hz)	30	0.6751
Zieliński et al. [17]	Channel connected spherical pores (SLA)	36	0.3911
	Channel connected spherical pores (CJP)	36	0.611
	Channel connected spherical pores (SLA)	48	0.4371
	Channel connected spherical pores (CJP)	48	0.6598
Wang et al. [16]	Kelvin cell	40	0.1786
	G7	40	0.2711
	ISO truss	40	0.2889
	Auxetic Hex	40	0.1799
Chua et al. [15]	SC-truss	30	0.1923
	BCC-truss	30	0.2091
	FCC-truss	30	0.2824
	Fluorite-truss	30	0.4121
Lomte et al. [7]	Orthogonal rods	50.8	0.8263
	Orthogonal rods	50.8	0.5098
	Orthogonal rods	50.8	0.4053

References

[1] T.J. Cox, P. D'Antonio, Acoustic Absorbers and Diffusers: Theory, Design and Application, 3rd edition, Taylor & Francis, London; New York, 2017.

[2] K. Gao, J.A.W. van Dommelen, M.G.D. Geers, Investigation of the effects of the microstructure on the sound absorption performance of polymer foams using a computational homogenization approach, Eur. J. Mech. A, Solids 61 (2017) 330–344, https://doi.org/10.1016/j.euromechsol.2016.10.011.

[3] O. Doutres, M. Ouisse, N. Atalla, M. Ichchou, Impact of the irregular microgeometry of polyurethane foam on the macroscopic acoustic behavior predicted by a unit-cell model, J. Acoust. Soc. Am. 136 (4) (2014) 1666–1681, https://doi.org/10.1121/1.4895695.

[4] S. Deshmukh, H. Ronge, S. Ramamoorthy, Design of periodic foam structures for acoustic applications: concept, parametric study and experimental validation, Mater. Des. 175 (2019) 107830, https://doi.org/10.1016/j.matdes.2019.107830.

[5] E.R. Fotsing, A. Dubourg, A. Ross, J. Mardjono, Acoustic properties of periodic microstructures obtained by additive manufacturing, Appl. Acoust. 148 (2019) 322–331, https://doi.org/10.1016/j.apacoust.2018.12.030.

[6] J. Boulvert, J. Costa-Baptista, T. Cavalieri, M. Perna, E.R. Fotsing, V. Romero-García, G. Gabard, A. Ross, J. Mardjono, J.-P. Groby, Acoustic modeling of micro-lattices obtained by additive manufacturing, Appl. Acoust. 164 (2020) 107244, https://doi.org/10.1016/j.apacoust.2020.107244.

[7] A. Lomte, Y. Xue, W. Johnston, G. Song, J.S. Bolton, B. Sharma, Acoustic modeling of three-dimensional-printed fibrous sound absorbers, J. Acoust. Soc. Am. 156 (6) (2024) 3757–3771, https://doi.org/10.1121/10.0034429.

[8] T.G. Zieliński, K.C. Opiela, P. Pawłowski, N. Dauchez, T. Boutin, J. Kennedy, D. Trimble, H. Rice, B. Van Damme, G. Hannema, R. Wróbel, S. Kim, S. Ghaffari Mosanenzadeh, N.X. Fang, J. Yang, B. Briere de La Hosseraye, M.C.J. Hornikx, E. Salze, M.-A. Galland, R. Boonen, A. Carvalho de Sousa, E. Deckers, M. Gaborit, J.-P. Groby, Reproducibility of sound-absorbing periodic porous materials using additive manufacturing technologies: round robin study, Addit. Manuf. 36 (2020) 101564, https://doi.org/10.1016/j.addma.2020.101564.

[9] W. Yang, J. An, C.K. Chua, K. Zhou, Acoustic absorptions of multifunctional polymeric cellular structures based on triply periodic minimal surfaces fabricated by stereolithography, Virtual Phys. Prototyp. 15 (2) (2020) 242–249, https://doi.org/10.1080/17452759.2020.1740747.

[10] H.J. Rice, J. Kennedy, P. Göransson, L. Dowling, D. Trimble, Design of a Kelvin cell acoustic metamaterial, J. Sound Vib. 472 (2020) 115167, https://doi.org/10.1016/j.jsv.2019.115167.

[11] X. Li, X. Yu, W. Zhai, Additively manufactured deformation-recoverable and broadband sound-absorbing microlattice inspired by the concept of traditional perforated panels, Adv. Mater. 33 (44) (2021) 2104552, https://doi.org/10.1002/adma.202104552.

[12] J. Li, D. Wang, Graded, M. Zhang, C. Liu, M. Deng, Y. Li, Graded minimal surface structures with high specific strength for broadband sound absorption produced by laser powder bed fusion, Coat. Mag. 13 (2023), https://doi.org/10.3390/coatings13111950.

[13] D.C. Akiwate, M.D. Date, B. Venkatesham, S. Suryakumar, Acoustic properties of additive manufactured narrow tube periodic structures, Appl. Acoust. 136 (2018) 123–131, https://doi.org/10.1016/j.apacoust.2018.02.022.

[14] X. Li, X. Yu, J.W. Chua, H. Lee, J. Ding, W. Zhai, Microlattice metamaterials with simultaneous superior acoustic and mechanical energy absorption, Small 17 (May 2021), https://doi.org/10.1002/smll.202100336.

[15] J.W. Chua, X. Li, X. Yu, W. Zhai, Novel slow-sound lattice absorbers based on the sonic black hole, Compos. Struct. 304 (2023) 116434, https://doi.org/10.1016/j.compstruct.2022.116434.

[16] Y. Wang, C. Li, X. Chen, C. Zhang, Q. Jin, G. Zhou, C. Wang, W. Zhao, Sound absorption performance based on auxetic microstructure model: a parametric study, Mater. Des. 232 (2023) 112130, https://doi.org/10.1016/j.matdes.2023.112130.

[17] T.G. Zieliński, N. Dauchez, T. Boutin, M. Leturia, A. Wilkinson, F. Chevillotte, F.-X. Bécot, R. Venegas, Taking advantage of a 3D printing imperfection in the development of sound-absorbing materials, Appl. Acoust. 197 (2022) 108941, https://doi.org/10.1016/j.apacoust.2022.108941.

[18] X. Li, J.W. Chua, X. Yu, Z. Li, M. Zhao, Z. Wang, W. Zhai, 3D-printed lattice structures for sound absorption: current progress, mechanisms and models, structural-property relationships, and future outlook, Adv. Sci. 11 (2023), https://doi.org/10.1002/advs.202305232.

[19] J. Allard, N. Atalla, Propagation of Sound in Porous Media: Modelling Sound Absorbing Materials, second edition, Wiley, 2009.

[20] T.G. Zieliński, R. Venegas, C. Perrot, M. Červenka, F. Chevillotte, K. Attenborough, Benchmarks for microstructure-based modelling of sound absorbing rigid-frame porous media, J. Sound Vib. 483 (2020) 115441, https://doi.org/10.1016/j.jsv.2020.115441.

[21] D.L. Johnson, J. Koplik, R. Dashen, Theory of dynamic permeability and tortuosity in fluid-saturated porous media, J. Fluid Mech. 176 (1987) 379–402, https://doi.org/10.1017/S0022112087000727.

[22] Y. Champoux, J. Allard, Dynamic tortuosity and bulk modulus in air-saturated porous media, J. Appl. Phys. 70 (4) (1991) 1975–1979, https://doi.org/10.1063/1.349482.

[23] D. Lafarge, P. Lemarinier, J.F. Allard, V. Tarnow, Dynamic compressibility of air in porous structures at audible frequencies, J. Acoust. Soc. Am. 102 (4) (1997) 1995–2006, https://doi.org/10.1121/1.419690.

[24] N. Jiménez, V. Romero-García, J.-P. Groby, Perfect absorption of sound by rigidly-backed high-porous materials, Acta Acust. Acust. 104 (3) (2018) 396–409, https://doi.org/10.3813/AAA.919183.

[25] N. Jiménez, V. Romero-García, A. Cebrecos, R. Picó, V.J. Sánchez-Morcillo, L.M. Garcia-Raffi, Broadband quasi perfect absorption using chirped multi-layer porous materials, AIP Adv. 6 (12) (2016) 121605, https://doi.org/10.1063/1.4971274.

[26] S. Mahasaranon, K.V. Horoshenkov, A. Khan, H. Benkreira, The effect of continuous pore stratification on the acoustic absorption in open cell foams, J. Appl. Phys. 111 (8) (2012) 084901, https://doi.org/10.1063/1.3701710.

[27] J. Boulvert, T. Cavalieri, J. Costa-Baptista, L. Schwan, V. Romero-García, G. Gabard, E.R. Fotsing, A. Ross, J. Mardjono, J.-P. Groby, Optimally graded porous material for broadband perfect absorption of sound, J. Appl. Phys. 126 (17) (2019) 175101, https://doi.org/10.1063/1.5119715.

[28] T. Cavalieri, J. Boulvert, G. Gabard, V. Romero-García, M. Escouflaire, J. Regnard, J.-P. Groby, Graded and anisotropic porous materials for broadband and angular maximal acoustic absorption, Materials 13 (20) (2020) 4605, https://doi.org/10.3390/ma13204605.

[29] J. Costa-Baptista, E.R. Fotsing, J. Mardjono, D. Therriault, A. Ross, Design and fused filament fabrication of multilayered microchannels for subwavelength and broadband sound absorption, Addit. Manuf. 55 (2022) 102777, https://doi.org/10.1016/j.addma.2022.102777.

[30] T. Cavalieri, J. Boulvert, L. Schwan, G. Gabard, V. Romero-Garcìa, J.-P. Groby, M. Escouflaire, J. Mardjono, Acoustic wave propagation in effective graded fully

anisotropic fluid layers, J. Acoust. Soc. Am. 146 (5) (2019) 3400–3408, https://doi.org/10.1121/1.5131653.
[31] G. Gautier, L. Kelders, J.P. Groby, O. Dazel, L. De Ryck, P. Leclaire, Propagation of acoustic waves in a one-dimensional macroscopically inhomogeneous poroelastic material, J. Acoust. Soc. Am. 130 (3) (2011) 1390–1398, https://doi.org/10.1121/1.3605530.
[32] F. Liu, Z. Mao, P. Zhang, D.Z. Zhang, J. Jiang, Z. Ma, Functionally graded porous scaffolds in multiple patterns: new design method, physical and mechanical properties, Mater. Des. 160 (2018) 849–860, https://doi.org/10.1016/j.matdes.2018.09.053.
[33] D.W. Abueidda, M. Bakir, R.K. Abu Al-Rub, J.S. Bergström, N.A. Sobh, I. Jasiuk, Mechanical properties of 3D printed polymeric cellular materials with triply periodic minimal surface architectures, Mater. Des. 122 (2017) 255–267, https://doi.org/10.1016/j.matdes.2017.03.018.
[34] J. Feng, J. Fu, X. Yao, Y. He, Triply periodic minimal surface (TPMS) porous structures: from multi-scale design, precise additive manufacturing to multidisciplinary applications, Int. J. Extrem. Manuf. 4 (2) (2022) 022001, https://doi.org/10.1088/2631-7990/ac5be6.
[35] E. Davoodi, H. Montazerian, R. Esmaeilizadeh, A.C. Darabi, A. Rashidi, J. Kadkhodapour, H. Jahed, M. Hoorfar, A.S. Milani, P.S. Weiss, A. Khademhosseini, E. Toyserkani, Additively manufactured gradient porous Ti–6Al–4V hip replacement implants embedded with cell-laden gelatin methacryloyl hydrogels, ACS Appl. Mater. Interfaces 13 (19) (2021) 22110–22123, https://doi.org/10.1021/acsami.0c20751.
[36] O. Al-Ketan, M. Ali, M. Khalil, R. Rowshan, K.A. Khan, R.K. Abu Al-Rub, Forced convection computational fluid dynamics analysis of architected and three-dimensional printable heat sinks based on triply periodic minimal surfaces, J. Therm. Sci. Eng. Appl. 13 (2) (2020), https://doi.org/10.1115/1.4047385.
[37] F.M. Baena-Moreno, M. González-Castaño, J.C. Navarro de Miguel, K.U.M. Miah, R. Ossenbrink, J.A. Odriozola, H. Arellano-García, Stepping toward efficient microreactors for CO2 methanation: 3D-printed gyroid geometry, ACS Sustain. Chem. Eng. 9 (24) (2021) 8198–8206, https://doi.org/10.1021/acssuschemeng.1c01980.
[38] X. Guan, J. Yang, E. Deckers, M. Hornikx, Computational characterization of functionally graded porous absorbers based on triply periodic minimal surfaces (TPMS), in: Proceedings of the 10th Convention of the European Acoustics Association Forum Acusticum 2023, European Acoustics Association, Turin, Italy, 2023, pp. 4939–4946.
[39] O. Al-Ketan, R.K. Abu Al-Rub, MSLattice: a free software for generating uniform and graded lattices based on triply periodic minimal surfaces, Mater. Des. Process. Commun. 3 (6) (2021) e205, https://doi.org/10.1002/mdp2.205.
[40] COMSOL Multiphysics Version 6.2, COMSOL AB, Stockholm, Sweden, 2023, http://www.comsol.com.
[41] V. Romero-García, G. Theocharis, O. Richoux, V. Pagneux, Use of complex frequency plane to design broadband and sub-wavelength absorbers, J. Acoust. Soc. Am. 139 (6) (2016) 3395–3403, https://doi.org/10.1121/1.4950708.
[42] V. Romero-García, G. Theocharis, O. Richoux, A. Merkel, V. Tournat, V. Pagneux, Perfect and broadband acoustic absorption by critically coupled sub-wavelength resonators, Sci. Rep. 6 (1) (2016) 19519, https://doi.org/10.1038/srep19519.
[43] fmincon documentation, The MathWorks Inc., Natick, Massachusetts, United States, 2024, https://nl.mathworks.com/help/optim/ug/fmincon.html.
[44] Z. Ugray, L. Lasdon, J. Plummer, F. Glover, J. Kelly, R. Marti, Scatter search and local NLP solvers: a multistart framework for global optimization, INFORMS J. Comput. 19 (2007) 328–340, https://doi.org/10.2139/ssrn.886559.
[45] D.E. Goldberg, Genetic Algorithms in Search, Optimization, and Machine Learning, Addison-Wesley, 1989.
[46] J. Kennedy, R. Eberhart, Particle swarm optimization, in: Proceedings of ICNN'95 - International Conference on Neural Networks, vol. 4, 1995, pp. 1942–1948.
[47] J. Nocedal, S.J. Wright, Numerical Optimization, Springer Series in Operations Research and Financial Engineering, Springer, New York, 2006.
[48] J.H. Park, J.S. Lee, Y.Y. Kim, Directional quantification of power dissipation in sound-absorbing metaporous layers, J. Sound Vib. 512 (2021) 116375, https://doi.org/10.1016/j.jsv.2021.116375.
[49] J. Carbajo, S. Ghaffari Mosanenzadeh, S. Kim, N.X. Fang, Sound absorption of acoustic resonators with oblique perforations, Appl. Phys. Lett. 116 (5) (2020) 054101, https://doi.org/10.1063/1.5132886.
[50] ISO 10534-2, Acoustics — Determination of Acoustic Properties in Impedance Tubes — Part 2: Two-Microphone Technique for Normal Sound Absorption Coefficient and Normal Surface Impedance, International Organization for Standardization, Geneva, Switzerland, 2023.
[51] J. Yang, J.S. Lee, Y.Y. Kim, Metaporous layer to overcome the thickness constraint for broadband sound absorption, J. Appl. Phys. (2015) 8, https://doi.org/10.1063/1.4919844.
[52] J. Yang, J.S. Lee, Y.Y. Kim, Multiple slow waves in metaporous layers for broadband sound absorption, J. Phys. D, Appl. Phys. 50 (1) (2016) 015301, https://doi.org/10.1088/1361-6463/50/1/015301.
[53] T. Cavalieri, J. Boulvert, V. Romero-García, G. Gabard, M. Escouflaire, J. Regnard, J.-P. Groby, Rapid additive manufacturing of optimized anisotropic metaporous surfaces for broadband absorption, J. Appl. Phys. 129 (11) (2021) 115102, https://doi.org/10.1063/5.0042563.